Contents

List of Figures

List of Tables

1 Event reconstruction

"Potentielle citation sans aucun rapport avec le sujet"

— Personne inconnue, *contexte à déterminer*

1.1 Charged particles track reconstruction

The track q is formed based on the information from the Inner Detector (ID) and contains five parameters: $q = (d_0, z_0, \phi, \theta, q/p)$, where d_0 is the distance from the track to the Z axis (transverse impact parameter), z_0 is the Z coordinate of the perpendicular dropped from the track onto the Z axis (longitudinal impact parameter) (see fig. 11), ϕ and θ are the azimuthal and polar angles correspondingly and q/p is the charge to momentum ratio of the particle. The process of the track reconstruction is the same for lepton and charged hadron candidates.

To form tracks using the detector response information the following steps are performed [2]:

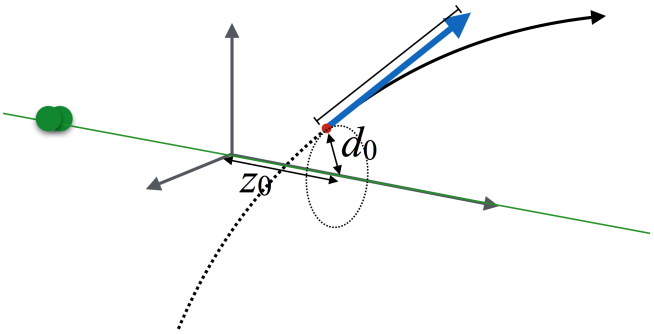

Figure 11: Impact parameters z_0 and d_0 [1].

- **Clustering** single hits in the pixel and SCT detectors. Neighbouring hits are combined to form a single cluster, clusters are then transformed into *space points* that have having 3D coordinates. A cluster may be identified as a single-particle cluster or as merged cluster, created by two or more particles. Identification of a cluster as a merged one and separation of energy deposits between the particles (possible only for two particles) is performed by means of a Neural Network (NN) algorithm.

- **Forming seeds** out of the space points. To form a seed three space-points originating from unique layers of the silicon detectors (pixel or SCT) are used. All possible combinations of seeds are formed at this stage. For every seed a crude estimate of the track parameters is performed.

- **Track candidates** are formed out of the seeds by extending them within the silicon sub-detectors following the most likely path. Combinatorial Kalman filter [3] is used to build the track candidates. The purity of the seeds depends significantly on the sub-detector that recorded the corresponding space-points. SCT-only seeds are considered the most reliable, followed the seeds that origin only from the pixel detector space-points, and the least reliable are the seeds originating from both of these sub-detectors - that determines the order of seed consideration when composing track candidates.
  Some fraction of the seeds that meet the necessary requirements become track candidates, the rest are discarded. A seed may be used for more than one track candidate if more than one space-point extension exists on the same layer.

- **Ambiguity solving** is the next step necessary to eliminate incorrectly assigned space-points or resolve conflicting track candidates that have and overlapping space-point. At this stage the track candidates are assigned a *track score*. The track score depends on the number of clusters associated to the track and which sub-detector these clusters originate from, the existence of holes (the absence of a cluster associated to a detector layer crossed by the track), the quality of the χ^2 fit of the track and track momentum.
  The tracks are ordered by their track score and consequently fed to the ambiguity resolving sequence. A truck must pass a number of kinematic cuts, impact parameters cuts, number of holes, number of clusters and shared clusters cuts, otherwise the track candidate is rejected. If a track candidate has no shared clusters with other candidates it is accepted after that. If there are merged clusters then it is up to the NN to either accept the track, reject it or eliminate a space-point and recycle the updated track candidate (see Fig. 12a).

- **TRT extension** means matching of the track, composed using the information from silicon sub-detectors to the trace in the TRT tracker. This allows to improve momentum measurement benefiting from extended track length.

- Final high-resolution **track fit** is performed using all available information. Position and uncertainty of each cluster are determined by an additional NN allowing for more precise track parameters. The curvature of the particle track also serves for charge sign identification.

1.2 Determining the primary vertex of the event

Primary vertex determination is crucial for physics analyses for many reasons. One of them is the necessity to separate particles originating from hard events from pile-up. Another reason is to keep

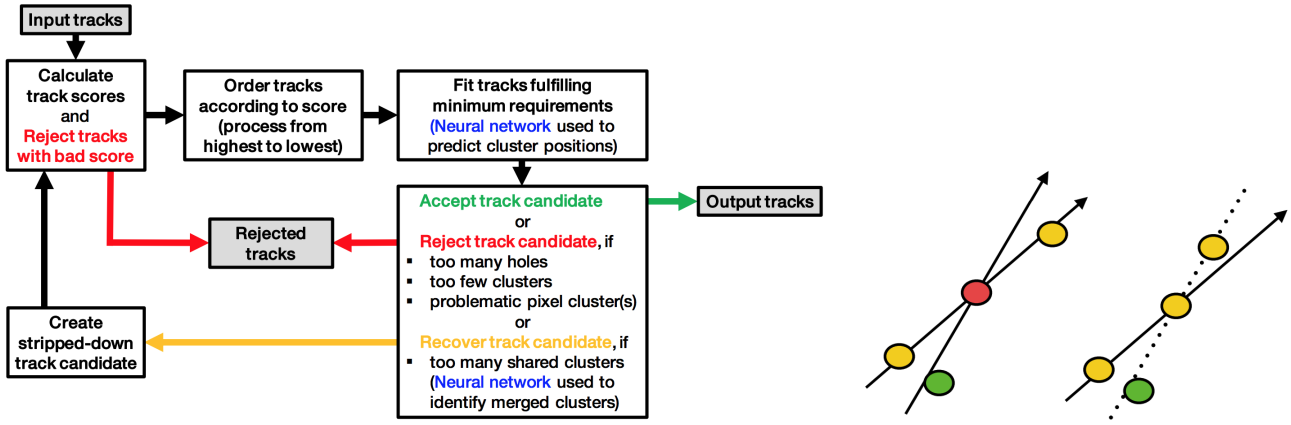

(a) Track ambiguity resolver algorithm.

(b) Tracks sharing space-points.

Figure 12: Ambiguity solving.

track of the decay chain and make difference between prompt and non-prompt particles. Flavour tagging, background suppression and decay reconstruction also rely heavily on the primary vertex determination.

After reconstructing the tracks of individual particles the obtained information is used to reconstruct the Primary Vertex (PV) of the event [4]. The procedure relies on the reconstructed tracks and goes as follows:

- A seed from the first vertex is selected. The transverse position of the seed is taken as a centre of the beam spot. The z-coordinate is the mode of z_0 coordinated of the tracks.

- Using the seed and the available tracks an iterative fit is performed in order to find the best position for the PV. In each iteration the tracks that are less compatible with the vertex are down-weighted and the vertex position gets recomputed. With every iteration the spread in the weight increases, separating track set into compatible tracks that mostly determine the vertex position and incompatible tracks that have little weight and therefore very little influence on the track position.

- After the fit is done compatible tracks remain assigned to the vertex, while incompatible tracks are removed from it. These incompatible tracks can be used in the determination of a different vertex.

- The procedure is repeated with the remaining tracks of the event.

For the upcoming Run 3 of the LHC certain improvements and modifications are foreseen [5].

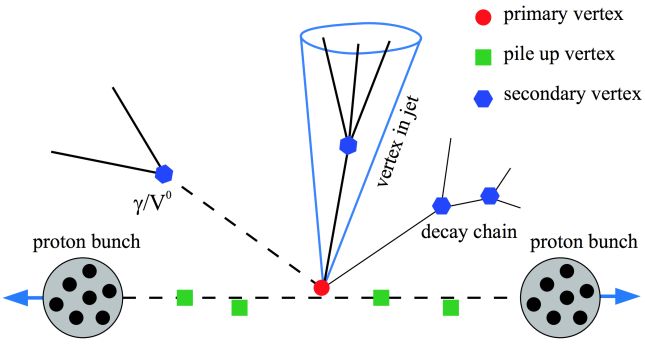

Figure 13: Primary, secondary and pile-up vertices [6].

1.3 Muon reconstruction and identification

Muon reconstruction relies primarily on the information from the ID (the muon track) and the Muon Spectrometer (MS), sometimes also using additional information from the calorimeter. At the first stage muon is independently reconstructed in the tracker and in the spectrometer, and then they are combined to compose a muon track used in the physics analyses [7]. Track reconstruction is described in subsection 1.1.

1.3.1 Muon reconstruction

Muon reconstruction on the muon spectrometer begins with a search for hit patterns in each muon chamber and forming of the segments. Using the Hough transform [8] the hits in each MDT chamber and nearby trigger chamber are aligned on trajectories in the bending plane. The orthogonal coordinate is measured with RPC and TGC detectors. A separate combinatorial search is conducted in the CSC detectors in ϕ and η detector planes.

Then the track candidates are built by fitting hits from different layers. This algorithm starts a combinatorial search first using the segments from the middle layers as seeds, as there are more trigger hits in the middle layer. The search is later extended to include the segments from other layers as seeds. Segment selection criteria are based on hit multiplicity and fit quality. The segments are matched using their relative positions and angles. In all the regions, except barrel-endcap transition region, at least two matching segments are needed to build a track (one segment is enough in the transition region). A single segment can be used by two or more track candidates. An overlap removal algorithm decides to which track should a segment belong or shares a segment between two tracks. A global χ^2 fit is used to fit all the hits associated to every track. If the χ^2 fit meets the designated criteria then the track is accepted. If a hit impair the χ^2 fit significantly, then this hit may be removed and the fit is repeated. On the other hand, new hits may be recovered if they fit the track candidate trajectory.
Accurate fitting of the track trajectory is extremely important for the measurement of muon momentum. A quantity called *sagitta* is measured by the MS (see Fig. 14). Knowing the length L and the sagitta S

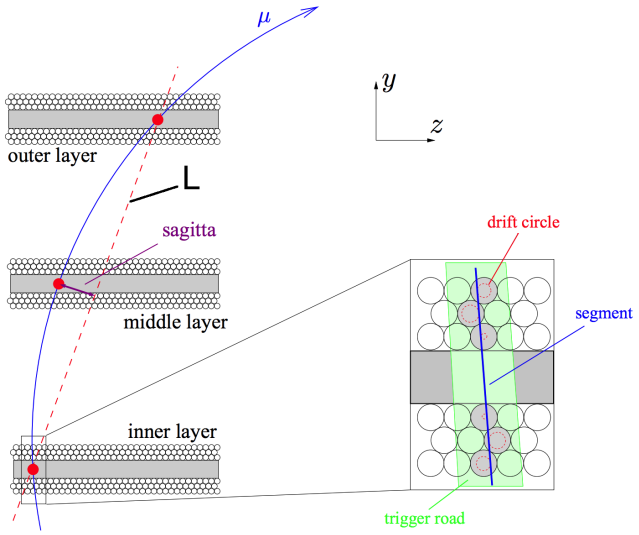

Figure 14: Sagitta used for the determination of the muon momentum [9].

we can determine the momentum:

$$p = \frac{BL^2}{8S}, \tag{1.1}$$

where B is the magnetic field strength.
After the muon gets reconstructed in every detector system separately, the obtained information is combined to form a reconstructed muon object. Depending on the detectors used for the combined reconstruction there are *four types of muons* defined (see Fig. 15):

- **Combined (CB) muon** is formed from a global refit of the tracks reconstructed independently in the ID and in the MS. During this global refit the hits from both detectors are used and also new hits may be added. Normally the outside-in pattern is used, when MS track is extrapolated inwards to match ID track. Inverse inside-out procedure is used as a complementary approach.

- **Segment-tagged (ST) muon** is a particle with an ID track that was extrapolated to the MS and associated with at least one local track segment in the MDT or CSC chambers. Normally these are muons with low p_T or their trajectory crosses regions with reduced MS acceptance.

- **Calorimeter-tagged (CT) muon** has a valid ID track that can be associated to an energy deposit in the calorimeter compatible with minimum-ionizing particle. The CT muons have the lowest purity among the muon types although they provide acceptance where the MS coverage may be absent, like the very central region with $|\eta| \leq 0.1$ for $15 < p_T < 100$ GeV.

- **Extrapolated (ME) muon** (standalone muon) trajectory is reconstructed base only on the MS track and a loose requirement to match the Interaction Point (IP). ME muons allow to extend the muon acceptance to the region which is not covered by the ID, namely $2.5 < |\eta| < 2.7$.

In case of overlap between different muon types the preference is given to CB muons, then to ST and then to CT muons. ME muons overlaps are resolved based on the MS track quality.

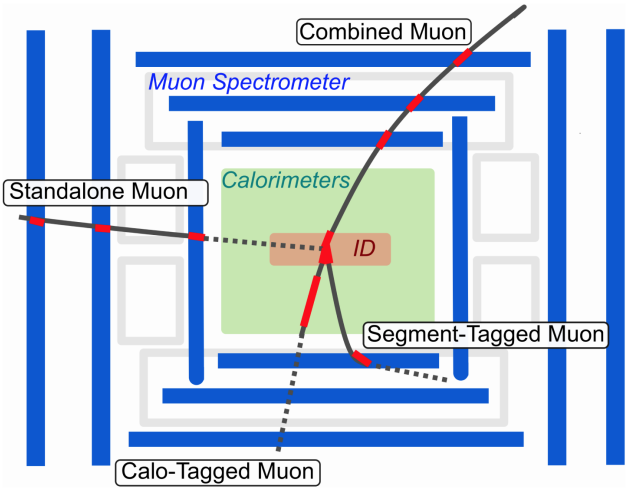

Figure 15: Four types of reconstructed muons.

1.3.2 Muon identification

Muon identification is a set of measures to ensure that the registered particle has indeed the characteristics of a muon and to identify the mechanism of its production. Muons created in the course of decay of a short-lived particle (e.g. a massive boson) are called *prompt muons*, while those originating from hadron or tau decays are called *non-prompt*. Muon identification plays an important role in background suppression and guaranteeing a robust momentum measurement.
Muons that are created during the in-flight decay of the charged hadrons in the ID usually have a distinctive "kink" topology in their reconstructed truck. This results in a decreased quality of the resulting track fit and the incompatibility between the results of momentum measurement in the ID and MS. Muons originating from W boson decays are called *signal*, while those coming from the hadron decays are called *background*. For CB muons the three main identification variables are the following:

- *q/p significance* is defined as $\frac{|(q/p)_{ID}-(q/p)_{MS}|}{\sqrt{\sigma^2(q/p)_{ID}+\sigma^2(q/p)_{MS}}}$ - an absolute difference between q/p measured in the two detectors over the combined uncertainty.
- Relative transverse momentum difference $\rho = \frac{|p_T^{ID}-p_T^{MS}|}{p_T^{combined}}$.
- Normalized χ^2 fit of the combined track.

Robust momentum measurement is ensured by specific requirements to the number of hits in the ID and MS. A number of muon identification selections (working points) is developed to address specific analyses.

1.3.3 Muon isolation

Isolated muons are a defining signature of massive boson decays. In the decays of W, Z and Higgs bosons muons are created separated from the rest of the particles. Quantitative measurement of detector activity around a muon candidate is called *muon isolation* and serves as an invaluable tool for background suppression. Muon isolation is assessed through two observables: one is track-based, another is calorimeter-based.

The track-based observable $p_T^{varcone30}$ is defined as a scalar sum of all the particles with $p_T > 1$ GeV in a cone $\Delta R = min(10GeV/p_T^{\mu}, 0.3)$ around the muon with transverse momentum p_T^{μ} excluding the proper track of the muon. The p_T dependence helps this definition to perform better for the muons created in the decay of the particles with high transverse momentum.

The calorimeter-based isolation observable $E_T^{topocone20}$ is defined as the sum of the transverse energy of all the topological clusters in a cone of a size $\Delta R = 0.2$ around the muon after subtracting the proper muon energy deposit and correcting for the pile-up effects.

Isolation criteria are normally defined using the relative isolation variables, using the ration of $p_T^{varcone30}$ and $E_T^{topocone20}$ to the transverse momentum. A number of working points exist, each having a certain requirements for one or both of the isolation variables.

1.4 Electron reconstruction and identification

1.4.1 Electron reconstruction

Electron reconstruction starts with two separate parts: track reconstruction in the ID and cluster reconstruction in the calorimeter, which are then matched to each other in order to make an electron candidate [10]. During Run 2 two algorithms were used for the cluster reconstruction, both of them are described below.

Sliding window

The electromagnetic calorimeter (EMC) is divided into a grid of 200x256 towers in $\eta \times \phi$ plane, each tower having a size of $\Delta\eta \times \Delta\phi = 0.025 \times 0.025$, reproducing the granularity of the second layer in the EMC. Energy deposits in all available calorimeter layers (first, second and third layers of the EMC in the region $|\eta| < 2.47$ and the presampler in the region $|\eta| < 1.8$) are approximately calibrated at the EM scale and summed up for each tower. If the cumulative energy deposit in a certain tower exceeds 2.5 GeV then this tower is used as a seed. Then for every seed a sliding window algorithm of size 3×5 is used [11], forming a cluster around every seed.

It happens that two seed-cluster candidates are found in close proximity. When their towers overlap

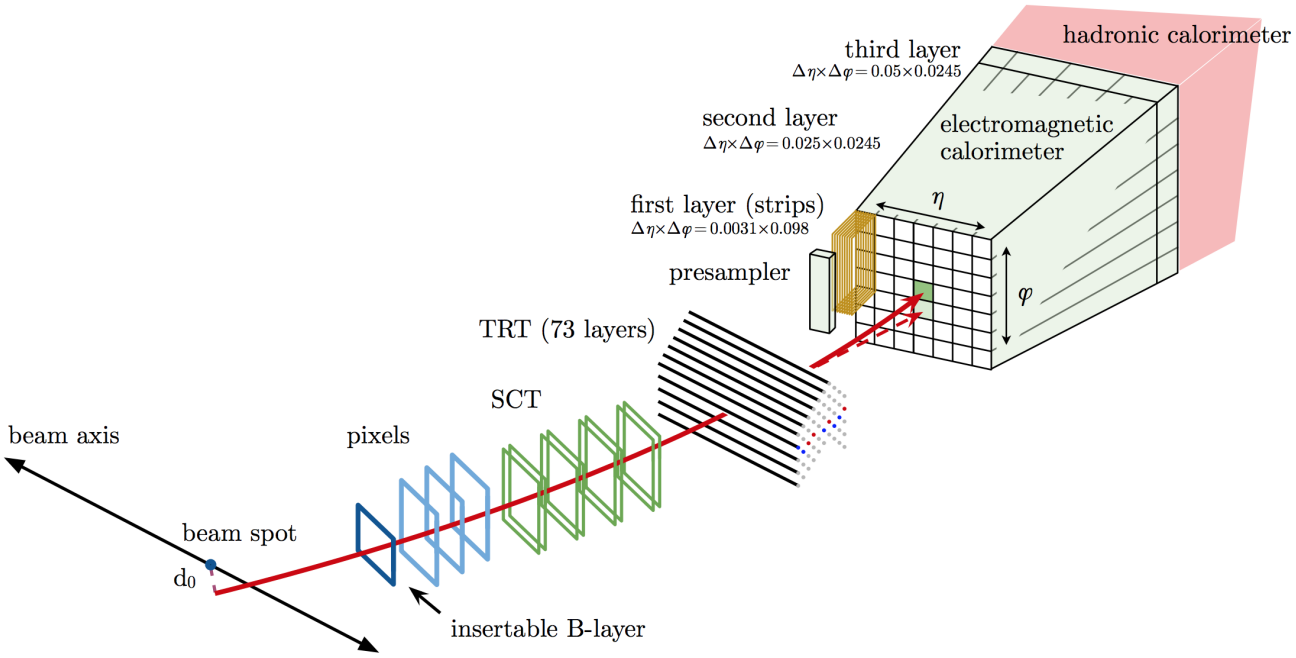

Figure 16: The path of an electron through the detector is shown by solid red line. The dashed red line denotes the trajectory of a photon, produced as a Bremsstrahlung radiation in the TRT.

within an area of $\eta \times \phi = 5 \times 9$ in units of 0.025×0.025 the two clusters are considered overlapping. In this case two options are possible:

- If the transverse energies of the two clusters are more than 10% different then the cluster with higher E_T is retained.
- If the difference in the transverse energies is within 10% then the cluster with higher value of the E_T in the central tower is kept.

After the overlap is resolved the duplicate cluster gets removed.

Topocluster reconstruction

The algorithm for topocluster reconstruction [12], [13] starts with composing proto-clusters in the calorimeter using the noise threshold:

$$\zeta_{cell}^{EM} = \frac{E_{cell}^{EM}}{\sigma_{noise,cell}^{EM}}, \tag{1.2}$$

where E_{cell}^{EM} is the cell energy at the EM scale and $\sigma_{noise,cell}^{EM}$ is the expected cell noise. The latter comprises of the electronic noise and pile-up noise estimate base on the expected instantaneous

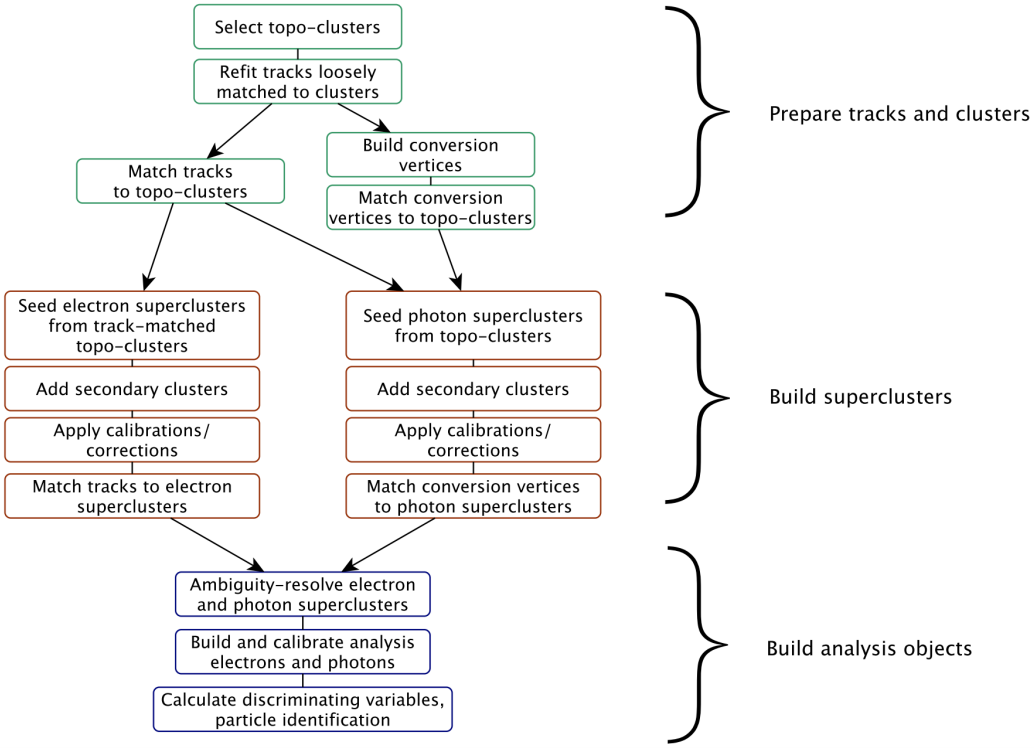

Figure 17: The algorithm scheme for topocluster reconstruction.

luminosity. The proto-cluster is formed around a cell with $|\zeta_{cell}^{EM} \geq 4|$. Then the neighbouring cell that pass the requirement of $|\zeta_{cell}^{EM} \geq 2|$ are added to the proto-cluster and serve as a seed for the next iteration, collecting all of its neighbours to the proto-cluster. If the two proto-clusters share a cell with $|\zeta_{cell}^{EM} \geq 2|$ then these proto-clusters are merged together. At every iteration neighbouring cells are added to the cluster even if they don't make the threshold. Proto-clusters with two local maxima are split into two clusters. For the proto-cluster to be considered as EM topocluster it must have at least 50% of its energy being contained in the EMC. At the stage of truck reconstruction the tracks are first extended and fitted with the global χ^2 fitter using the pion hypothesis [14]. If it fails, then a more complicated pattern reconstruction algorithm based on Kalman filter is used [15]. This algorithm uses the electron hypothesis and allows up to 30% energy loss at each material surface. Then the tracks are loosely matched to the EM clusters if they meet one of the following criteria:

- The tracks extrapolated to the second layer of the EMC are consistent in ϕ and η (matching in η is not required for TRT-only tracks).

- The extrapolated tracks are consistent in ϕ (with a bit tighter requirements) and η after rescaling the track momentum to cluster momentum.

Track-cluster matching

Matching in ϕ coordinate assumes charge asymmetry to account for different direction of possible Bremsstrahlung radiation for positive and negative particles. Then the loosely matched tracks that have at least four silicon hits are refitted using the optimized Gaussian-sum filter (GSF) [16], that allows to better take into account the energy losses in solid material.
After the track is fitted with the GSF algorithm the final matching with the cluster is performed using tighter matching requirements between the track and the cluster barycentre. If matching criteria are met with two or more tracks then an ambiguity resolving algorithm is used. This algorithm takes into account a number of parameters like the distance between the cluster barycentre and the track in ϕ and η, number of hits in the silicon detector and in the innermost silicon layer, association to photon conversion vertex, E/p ration and p_T. This allows to rule out converted photons as electron candidates and also helps to maintain high photon reconstruction efficiency. After track-cluster matching the electron cluster is extended around the seed to 3×7 in the barrel region or 5×5 in the end-cap region by adding one row of the cells on each side.

Supercluster reconstruction

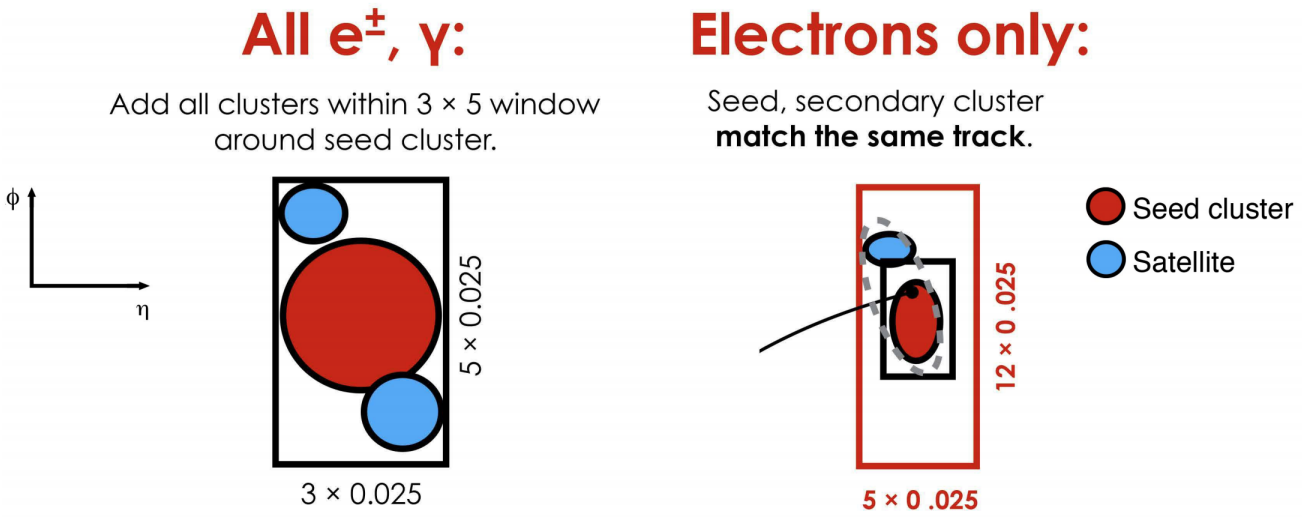

Figure 18: Supercluster reconstruction for electrons. Seed clusters are shown in red, satellite clusters in blue.

The composition of electron supercluster is performed in two stages: first, the candidate EM topocluster is tested to be used as a seed for the supercluster. In the second stage the nearby EM topoclusters can be identified as satellite clusters, emerging from Bremsstrahlung radiation or topocluster splitting. First the EM topoclusters are sorted by their E_T in descending order. For the cluster to be considered a seed it must have the $E_T > 1$ GeV, must be matched to a truck with at least for hits in the silicon

detectors and should not be assigned as a satellite cluster to any other seed. If these requirements are met then the algorithm described in Fig. 18 is started. First, all topoclusters within a window of $\Delta\eta \times \Delta\phi = 0.075 \times 0.125$ around the seed cluster barycentre are added as satellite cluster, as they most probably represent secondary EM showers coming from the same initial electron. Also, if a cluster within $\Delta\eta \times \Delta\phi = 0.125 \times 0.3$ window around the seed cluster barycentre share the "best-matched" track with the seed cluster - it is also added as a satellite. Finally the energy of the reconstructed cluster must be calibrated. The calibration is performed using the multivariate technique based on data and MC samples using $Z \rightarrow ee$ events [17], [18]. The shower shapes and other discriminating variables are computed at this stage.

1.4.2 Electron identification

Prompt electrons in the central region of the ATLAS detector ($|\eta| < 2.47$) are selected using a likelihood-based (LH) identification. The LH uses a number of inputs from ID and calorimeter detectors, as well as combined information from both detectors (see Table 1 in [10]). The probability density functions (pdfs) for the likelihoods of Run 2 were obtained using the simulated events.
The electron LH is based on the products of n pdfs P for signal L_S and background L_B:

$$L_{S(B)}(\mathbf{x}) = \prod_{i=1}^{n} P^i_{S(B)}(x_i), \tag{1.3}$$

where $\mathbf{x}$ is the vector of the LH input parameters, P^i_S and P^i_B are the pdf values for parameter i at value x_i for signal and background respectively. The LH operates at a number of working points, the higher the likelihood - the lower is the efficiency. For example, the efficiencies for identifying a prompt electron with $E_T = 40$ GeV for Loose, Medium and Tight working points are 93%, 88% and 80% respectively. Prompt electrons are assumed to be the signal, while background includes the jets that mimic the prompt electrons, electrons from photon conversions and non-prompt electrons from hadron decays. For each electron candidate a discriminant d_L is composed:

$$d_L = \frac{L_S}{L_S + L_B}, \tag{1.4}$$

that defines the electron likelihood identification. This discriminant d_L has a sharp peak at unity for the signal and at zero for the background, which is not very convenient for picking working points. That is why the discriminant distribution is transformed using the inverse sigmoid function:

$$d'_L = -\tau^{-1} \ln (d_L^{-1} - 1), \tag{1.5}$$

where $\tau = 15$. Each operating point is assigned with a d'_L value - if a discriminant exceeds this value for a given electron then this electron is considered signal.
There are two advantages of using likelihood-based approach comparing to selection-criteria-based ("cut-based") identification:

- The drawback of a cut-based approach is that if an electron fails to pass one of the cuts - it is definitely removed from the selection, while in the LH approach it is still possible for this electron to pass the selection thanks to other parameters. This quality promotes the selection efficiency.

- In case of a significant overlap in signal and background distribution of a certain parameter using it in a cut-based identification would entail large losses in efficiency. In the likelihood-based identification this parameter may be added without penalty.

The likelihood input parameters were obtained from the simulated events, which means that real distributions in data may differ due to various mismodelling effects. These effects must be corrected in order to get the accurate and efficient identification. Mismodelling may depend on coordinates or energy. Chapter **??** of this dissertation is devoted to correction of electromagnetic shower shapes in the calorimeter, which are among the likelihood input parameters.

1.4.3 Electron isolation

Electron isolation plays a very important role in background suppression in physics analyses. Since electrons are reconstructed using the information from two different detectors - two different isolation definitions are possible, track-based and calorimeter-based. Let's first consider calorimeter-based isolation.

As depicted in Fig. 19 the raw isolation energy $E_{isol}^{T,raw}$ includes the energy of all the topoclusters,

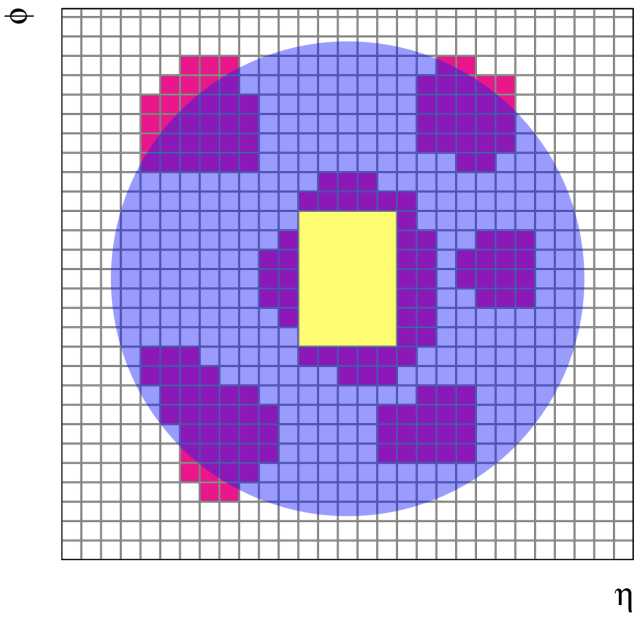

Figure 19: The isolation cone is centred at the candidate electron. All topological clusters, shown in red, are included in the raw isolation variable. The 5×7 cells included into core subtraction method are marked in yellow.

barycentres of which fall within the isolation radius ΔR. It also includes core energy of the electron candidate $E_{isol}^{T,core}$ which comprises the 5×7 cells within the area of $\Delta\eta \times \Delta\phi = 0.125 \times 0.175$. The fixed size of the core ensures simplicity and stability, although it may happen that the topocluster is larger than the size of the core resulting in attributing the proper energy of the electron to the outside activity. This leakage effect is corrected for using no pile-up simulated events, parametrizing the leakage with a Crystal Ball function as a function of the transverse energy $E_{T,leakage} = E_{T,leakage}(E_T)$.
Another effect that must be corrected for is the pile-up and underlying event contribution. This contribution is estimated from from the ambient energy density [19]. This implies the calculation of the median energy density $\rho_{median}(\eta)$ - a rapidity-dependent estimate of jet densities for every event. Then the pile-up correction can be evaluated in the following way:

$$E_{T,pile-up}(\eta) = \rho_{median}(\eta) \times (\pi\Delta R^2 - A_{core}), \tag{1.6}$$

where ΔR is the radius of the isolation cone, and A_{core} is the area of the subtracted signal core. Finally the calorimeter isolation variable may be defined as follows:

$$E_{T,cone}^{isol} = E_{T,raw}^{isol} - E_{T,core} - E_{T,leakage} - E_{T,pile-up}. \tag{1.7}$$

The track-based isolation includes all tracks with $p_T > 1$ GeV within a fiducial region of the ID that satisfy basic track quality requirements. Pile-up is mitigated by requiring that $|z_0 \sin\theta| < 3$ mm, to ensure that the track points at the primary vertex. The track-based isolation is composed of all the tracks that fall within the radius ΔR excluding the candidate electron track.
The own contribution of the candidate track into the isolation must also include possible Bremsstrahlung radiation emitted by the candidate electron. For that reason the tracks are extrapolated to the second layer of the EMC and if they fall within a window of $\Delta\eta \times \Delta\phi = 0.05 \times 0.1$ around the cluster position. The resulting variable is called p_T^{isol}.
The track-based isolation allows to use variable-size cone, making the cone smaller for boosted particles. The cone size for the $p_{T,var}^{isol}$ would be:

$$\Delta R = min\left(\frac{10GeV}{p_T[GeV]}, R_{max}\right), \tag{1.8}$$

where R_{max} is the maximum cone size and may vary depending on the analysis needs, typically between 0.2 and 0.4.

1.5 Particle flow objects

The measurement of hadronic objects and particle showers remains a complicated task due to large variety of particle types and properties they posses and because of the large energy/momentum span of the measured objects. For the low-energy charged particles the ID shows better momentum resolution and angular resolution. On the other hand, the calorimeter shows better performance at high energy

and is also capable of detecting neutral particles. The idea behind the Particle Flow (PF) algorithm [20] is to combine the information from the two detectors to obtain the best result possible. To properly take into account every particle it has to be ensured that every particle detected in both detectors is counted only once. This means that for a charged particle its deposit in the calorimeter must be found and subtracted. The Particle Flow Object (PFO) reconstruction process is schematically presented in Fig. 110. The process starts with getting *tight* tracks from the ID, meaning these tracks must have at

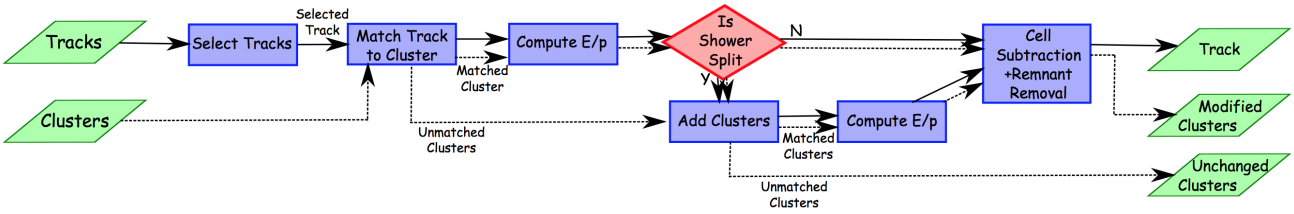

Figure 110: The algorithm scheme for particle flow object reconstruction.

least nine hits in the silicon detectors and no holes n the pixel detector. The tracks must have $|\eta| < 2.5$ and $0.5 < p_T < 40$ GeV, corresponding to the kinematic region where tracks offer better resolution than the calorimeter. The tracks associated to leptons are removed.

The calorimeter topoclusters reconstructed like it was described in section 1.4.1 and calibrated using the EM scale are matched to the tracks based on their spacial position and measured momentum. First the ranked based on a distance metric:

$$\Delta R' = \sqrt{\left(\frac{\Delta\phi}{\sigma_\phi}\right)^2 + \left(\frac{\Delta\eta}{\sigma_\eta}\right)^2}, \tag{1.9}$$

where $\Delta\phi$ and $\Delta\eta$ are the angular distances between the topocluster barycentres and the track, σ_ϕ and σ_η are uncertainties in topocluster width. Preliminary matching is reached by requiring that $E^{clus}/p^{trk} > 0.1$, where E^{clus} is the cluster energy and p^{trk} is the track momentum.

It often happens, that energy deposit of a particle is split between two (most often) or more clusters. Then a split shower recovery procedure is initiated, looking for matching clusters in the radius of $\Delta R = 0.2$ around the track extrapolated to the second layer of the EMC. Then it is estimated if the energy of the track and the energy of the associated topocluster is consistent. If it is the case then the topoclusters matched to the tracks are removed.

Eventually two particle collections are obtained: a collection of charged particle flow objects (cPFOs) each with an associated track and neutral particle flow objects (nPFOs) with a calorimeter deposit. The former must also match the primary vertex, having $|z_0 \times \sin\theta| < 2$ mm.

Bibliography

[1] "Performance of the ATLAS Silicon Pattern Recognition Algorithm in Data and Simulation at $\sqrt{s} = 7$ TeV". In: (July 2010).

[2] M. Aaboud et al. "Performance of the ATLAS Track Reconstruction Algorithms in Dense Environments in LHC Run 2". In: *Eur. Phys. J. C* 77.10 (2017), p. 673. DOI: 10.1140/epjc/s10052-017-5225-7. arXiv: 1704.07983 [hep-ex].

[3] R. Fruhwirth. "Application of Kalman filtering to track and vertex fitting". In: *Nucl. Instrum. Meth. A* 262 (1987), pp. 444–450. DOI: 10.1016/0168-9002(87)90887-4.

[4] S. Boutle et al. "Primary vertex reconstruction at the ATLAS experiment". In: *J. Phys. Conf. Ser.* 898.4 (2017). Ed. by Richard Mount and Craig Tull, p. 042056. DOI: 10.1088/1742-6596/898/4/042056.

[5] *Development of ATLAS Primary Vertex Reconstruction for LHC Run 3*. Tech. rep. ATL-PHYS-PUB-2019-015. Geneva: CERN, Apr. 2019. URL: https://cds.cern.ch/record/2670380.

[6] E. Bouhova-Thacker et al. "Vertex reconstruction in the ATLAS experiment at the LHC". In: *2008 IEEE Nuclear Science Symposium and Medical Imaging Conference and 16th International Workshop on Room-Temperature Semiconductor X-Ray and Gamma-Ray Detectors*. 2008, pp. 1720–1727. DOI: 10.1109/NSSMIC.2008.4774734.

[7] Georges Aad et al. "Muon reconstruction performance of the ATLAS detector in proton–proton collision data at $\sqrt{s}$ =13 TeV". In: *Eur. Phys. J. C* 76.5 (2016), p. 292. DOI: 10.1140/epjc/s10052-016-4120-y. arXiv: 1603.05598 [hep-ex].

[8] J. Illingworth and J. Kittler. "A survey of the hough transform". In: *Computer Vision, Graphics, and Image Processing* 44.1 (1988), pp. 87–116. ISSN: 0734-189X. DOI: https://doi.org/10.1016/S0734-189X(88)80033-1. URL: http://www.sciencedirect.com/science/article/pii/S0734189X88800331.

[9] Steffen Kaiser. "Search for the Higgs Boson in the Process $pp \to Hqq$, $H \to WW$ with the ATLAS Detector". PhD thesis. Munich, Technische Universitaet Muenchen, 2010.

[10] Morad Aaboud et al. "Electron reconstruction and identification in the ATLAS experiment using the 2015 and 2016 LHC proton-proton collision data at $\sqrt{s} = 13$ TeV". In: *Eur. Phys. J. C* 79.8 (2019), p. 639. DOI: 10.1140/epjc/s10052-019-7140-6. arXiv: 1902.04655 [physics.ins-det].

[11] W Lampl et al. *Calorimeter Clustering Algorithms: Description and Performance*. Tech. rep. ATL-LARG-PUB-2008-002. ATL-COM-LARG-2008-003. Geneva: CERN, Apr. 2008. URL: https://cds.cern.ch/record/1099735.

[12] Georges et al. Aad. "Topological cell clustering in the ATLAS calorimeters and its performance in LHC Run 1. Topological cell clustering in the ATLAS calorimeters and its performance in LHC Run 1". In: *Eur. Phys. J. C* 77.CERN-PH-EP-2015-304 (Mar. 2016). Comments: 64 pages plus author list + cover page (87 pages in total), 41 figures, 3 tables, submitted to EPJC. All figures including auxiliary figures are available at http://atlas.web.cern.ch/Atlas/GROUPS/PHYSICS/PAPERS/PERF-2014-07/, 490. 87 p. DOI: 10.1140/epjc/s10052-017-5004-5. URL: https://cds.cern.ch/record/2138166.

[13] Georges Aad et al. "Electron and photon performance measurements with the ATLAS detector using the 2015–2017 LHC proton-proton collision data". In: *JINST* 14.12 (2019), P12006. DOI: 10.1088/1748-0221/14/12/P12006. arXiv: 1908.00005 [hep-ex].

[14] Thijs G. Cornelissen et al. "The global chi**2 track fitter in ATLAS". In: *J. Phys. Conf. Ser.* 119 (2008). Ed. by Randall Sobie, Reda Tafirout, and Jana Thomson, p. 032013. DOI: 10.1088/1742-6596/119/3/032013.

[15] T Cornelissen et al. *Concepts, Design and Implementation of the ATLAS New Tracking (NEWT)*. Tech. rep. ATL-SOFT-PUB-2007-007. ATL-COM-SOFT-2007-002. Geneva: CERN, Mar. 2007. URL: https://cds.cern.ch/record/1020106.

[16] *Improved electron reconstruction in ATLAS using the Gaussian Sum Filter-based model for bremsstrahlung*. Tech. rep. ATLAS-CONF-2012-047. Geneva: CERN, May 2012. URL: https://cds.cern.ch/record/1449796.

[17] Morad Aaboud et al. "Electron and photon energy calibration with the ATLAS detector using 2015–2016 LHC proton-proton collision data". In: *JINST* 14.03 (2019), P03017. DOI: 10.1088/1748-0221/14/03/P03017. arXiv: 1812.03848 [hep-ex].

[18] Morad Aaboud et al. "Measurement of the photon identification efficiencies with the ATLAS detector using LHC Run 2 data collected in 2015 and 2016". In: *Eur. Phys. J. C* 79.3 (2019), p. 205. DOI: 10.1140/epjc/s10052-019-6650-6. arXiv: 1810.05087 [hep-ex].

[19] Matteo Cacciari and Gavin P. Salam. "Pileup subtraction using jet areas". In: *Phys. Lett. B* 659 (2008), pp. 119–126. DOI: 10.1016/j.physletb.2007.09.077. arXiv: 0707.1378 [hep-ph].

[20] Morad et al. Aaboud. "Jet reconstruction and performance using particle flow with the ATLAS Detector. Jet reconstruction and performance using particle flow with the ATLAS Detector". In: *Eur. Phys. J. C* 77.CERN-EP-2017-024. 7 (Mar. 2017). 67 pages in total, author list starting page 51, 37 figures, 1 table, final version published in Eur. Phys. J C, all figures including auxiliary figures are available at http://atlas.web.cern.ch/Atlas/GROUPS/PHYSICS/PAPERS/PERF-2015-09/, 466. 67 p. DOI: 10.1140/epjc/s10052-017-5031-2. URL: https://cds.cern.ch/record/2257597.